



UvA-DARE (Digital Academic Repository)

Bending benzenes and twisting light

Kovida, K.

Publication date
2026

[Link to publication](#)

Citation for published version (APA):

Kovida, K. (2026). *Bending benzenes and twisting light*. [Thesis, fully internal, Universiteit van Amsterdam].

General rights

It is not permitted to download or to forward/distribute the text or part of it without the consent of the author(s) and/or copyright holder(s), other than for strictly personal, individual use, unless the work is under an open content license (like Creative Commons).

Disclaimer/Complaints regulations

If you believe that digital publication of certain material infringes any of your rights or (privacy) interests, please let the Library know, stating your reasons. In case of a legitimate complaint, the Library will make the material inaccessible and/or remove it from the website. Please Ask the Library: <https://uba.uva.nl/en/contact>, or a letter to: Library of the University of Amsterdam, Secretariat, P.O. Box 19185, 1000 GD Amsterdam, The Netherlands. You will be contacted as soon as possible.

3

Role of Exciton Delocalization in Chiroptical Properties of Benzothiadiazole Carbon Nanohoops

This chapter has been published as: Kovida K.; Malinčík J.; Cruz C.M.; Campaña A.G., Šolomek T. Role of Exciton Delocalization in Chiroptical Properties of Benzothiadiazole Carbon Nanohoops. *Chem. Sci.*, 2025, **16**, 1405-1410.

Abstract

Development of chiral organic materials with a strong chiroptical response is crucial to advance technologies based on circularly polarized luminescence, enantioselective sensing, or unique optical signatures in anti-counterfeiting. The progress in the field is hampered by the lack of structure–property relationships that would help designing new chiral molecules. Here, we address this challenge by synthesis and investigation of two chiral macrocycles that integrate in their structure a pseudo-meta [2.2]paracyclophane with planar chirality and a highly fluorescent benzothiadiazole. Both compounds display remarkably red-shifted fluorescence with high quantum yields and large Stokes shifts. They differ in the extent of p-electron conjugation that allowed, for the first time, systematic examination of the effect of exciton delocalization on the absorption and luminescence of circularly polarized light. By a combination of steady-state spectroscopy and quantum chemical calculations, we constructed a unique structure–property relationship offering critical insights that will aid and abet the development of robust design guidelines for materials with strong electronic circular dichroism or circularly polarized luminescence of exceptional brightness.

3.1 Introduction

Organic materials with strong electronic circular dichroism (ECD) and circularly polarized luminescence (CPL) are attractive synthetic targets for their potential applications in chiroptical devices.^{1–5} The quality of such chiroptical materials is determined by a few key metrics: the dissymmetry factor (g), the molar absorptivity (ϵ), and the fluorescence quantum yield (ϕ_F).^{6,7} Combined, they define the overall brightness of CPL, B_{CPL} .⁸ The typical values of the luminescence dissymmetry factor (g_{lum}) in small organic molecules are relatively low. The dissymmetry factor critically depends on the size and mutual orientation of the electric (μ) and magnetic (m) transition dipole moments and, as a result, it is relatively difficult to tune systematically by precision organic synthesis due to absence of robust molecular design guidelines. For example, among the few known to improve g_{lum} is imposing the D_n symmetry^{9,10} to a chiral fluorophore, as demonstrated in a figure-eight-shaped [5]helicene dimer by Matsuda and Hirose.¹¹ Here, the electric and magnetic transition dipole moments adopt ideal parallel orientation providing $|g_{\text{lum}}| = 1.5 \times 10^{-2}$. However, this system suffers from a relatively low ϕ_F , *i.e.*, low μ . Similarly, high absorption dissymmetry factor (g_{abs}) in ECD is often associated with lower molar absorptivity, with the latter further impacting B_{CPL} . Although the underlying theory is well-established,^{7,10,12} systematic studies on how the nature of the excited state transitions in CPL-active compounds depend on the molecular structure are relatively scarce.^{13–16} Recently, some of us proposed a rationalization for enhancing the $|m|$ in helically chiral compounds to achieve high values of g in ECD or CPL by finding a direct relationship with the area of the inner cavity of the helix.¹⁷

In recent years, chiral carbon nano hoops, π -conjugated macrocycles derived from cycloparaphenylenes ([n]CPPs) emerged as a promising class of CPL-active molecules. Curved architecture of CPPs endows them with visible-light fluorescence with relatively high ϕ_F that can be tuned by controlling their size with synthesis.^{18–21} But CPPs are achiral. Therefore, chirality in carbon nano hoops is typically induced by an incorporation of a chiral unit into CPPs, such as biphenyl, binaphthyl, helicene or others.^{22–30} Although they provide chiral nano hoops with a relatively high configurational stability, they can in principle racemize. Racemization can be fully prevented by creating topologically chiral carbon nano hoops as reported for example by Stepień or Jasti.^{31,32} Recently, Jiang *et al.* used planar chiral *pseudo-meta* [2.2]paracyclophane (PCP) to induce stable chirality and CPL response in carbon nano hoops, such as **1** (Figure 3.1),³³ and also used tetrasubstituted PCP to synthesize a topologically chiral carbon nano hoop.³⁴

CPPs emitting light above 500 nm display a low ϕ_F ,²¹ a key metric of a good fluorophore. In 2020, Jasti *et al.* reported an achiral benzothiadiazole (BT) nano hoop BT[10]CPP (Figure 3.1) with λ_{\max} at 571 nm, *i.e.*, with >100 nm red-shift compared to [10]CPP, and impressive $\phi_F = 0.59$.³⁵ However, chiral nano hoops with CPL with $\lambda_{\max} > 550$ nm and high ϕ_F are only rarely reported.³⁶

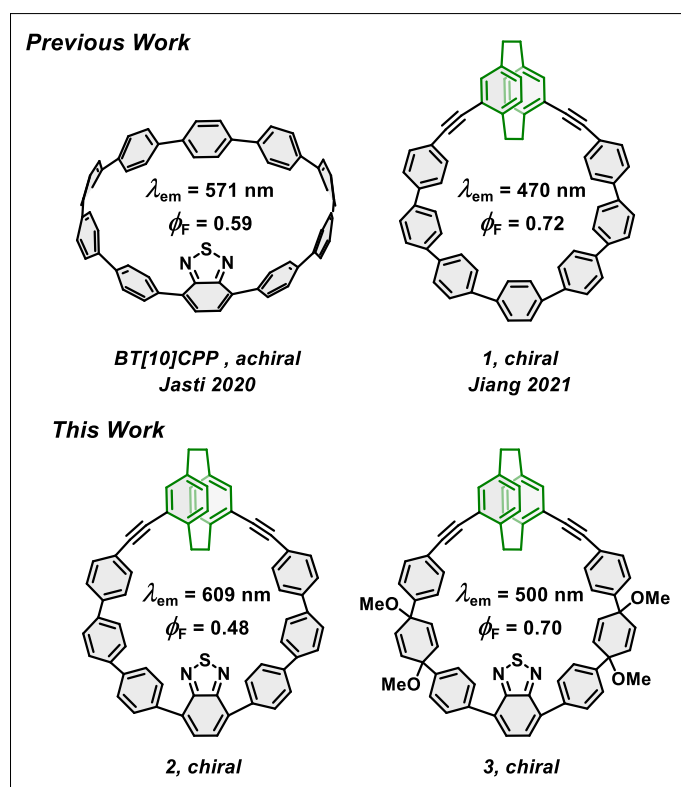
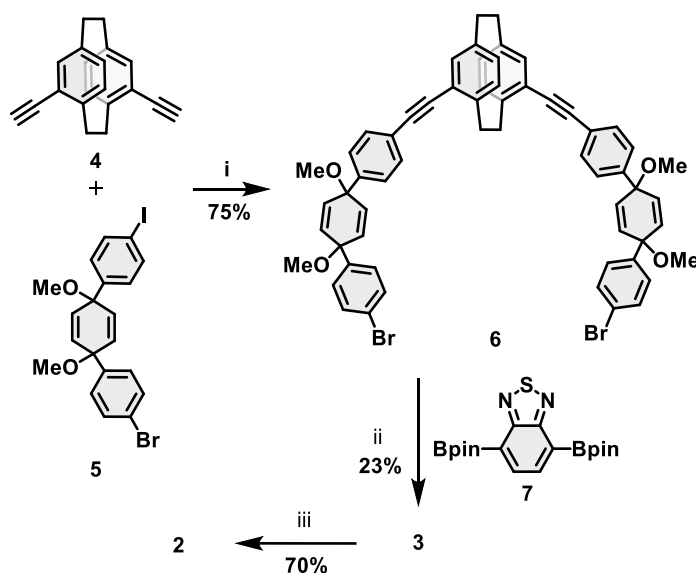


Figure 3.1. Examples of reported nano hoops (top) and present work (bottom).^{33,35}

Here, we report on simultaneous integration of *pseudo-meta* PCP and BT into a carbon nano hoop (**2**, Figure 3.1) accomplishing a CPL beyond 600 nm with a good ϕ_F . In addition, we achieved a turn-off of the π -electron conjugation in **2** using the pro-aromatic units in its equally luminous chiral precursor **3**. Compound **3** displayed a bright fluorescence at 500 nm, the first such nano hoop precursor to do so. Ultimately, the chiroptical properties of **1**, **2**, and **3** allowed us to explore, for the first time, the effect of the extent of exciton delocalization in this important class of molecules on their chiroptical response in ECD and CPL. The structure–property relationship constructed in this work together with the previous studies allowed us to formulate guidelines to aid the synthesis of new molecular systems with outstanding chiroptical properties.

3.2 Results and Discussion

Synthesis of target molecules: The target chiral carbon nanohoop **2** was synthesized according to the strategy developed by Jasti,¹⁸ *i.e.*, via aromatization of macrocycle **3** with pro-aromatic cyclohexa-2,5-dienyl units prepared according to Scheme 3.1. First, Sonogashira cross coupling between 4,15-bis(ethynyl)[2.2]paracyclophane **4** and building block **5** provided the C-shape intermediate **6**³³ in 75% yield. The Suzuki cross-coupling of **6** with **7** gave chiral macrocycle **3** in 23% yield. Reductive aromatization of **3** using SnCl₂/HCl lead to the desired nanohoop **2** alongside several side products, a result of acid-catalysed rearrangement reactions. Under these conditions, **2** was obtained as a bright fluorescent orange solid in 60% yield.



Scheme 3.1. Synthesis of BT containing macrocycles **2** and **3**. Reaction conditions: (i) Pd₂dba₃, PPh₃, CuI, THF/TEA, RT, 4h. (ii) K₃PO₄, SPhos Pd Gen 3, dioxane, 80 °C, 18 h (iii) A: SnCl₂, HCl, THF, RT, 2 h or B: Na, naphthalene, THF, -78 °C, 10 min

Reductive aromatization of **3** using SnCl₂/HCl lead to the desired nanohoop **2** alongside several side products, a result of acid-catalysed rearrangement reactions. Under these conditions, **2** was obtained as a bright fluorescent orange solid in 60% yield. We also conducted the aromatization using sodium naphthalenide as the reducing agent. In this case, nanohoop **2** was formed in a markedly cleaner process in 70% yield after purification by column chromatography. All compounds were fully characterized by ¹H, ¹³C NMR and high-resolution mass spectrometry (Figure A3.1–A3.6).

Photophysical properties of target compounds: We then investigated the optoelectronic properties of **2** and **3**. Note that the pro-aromatic cyclohexa-2,5-dienyls in **3** interrupt the π -electron conjugation between PCP and BT in the macrocycle, thereby preventing the unique optoelectronic properties of fully conjugated carbon nanohoop to emerge. Nevertheless, **3** displays a bright green fluorescence, which is highly unusual in macrocyclic precursors of carbon nanohoops. Here, the observed green luminescence in **3** allowed us to investigate how the conjugation affects the absorption and emission in these macrocycles (Figure 3.2a, Table 3.1).

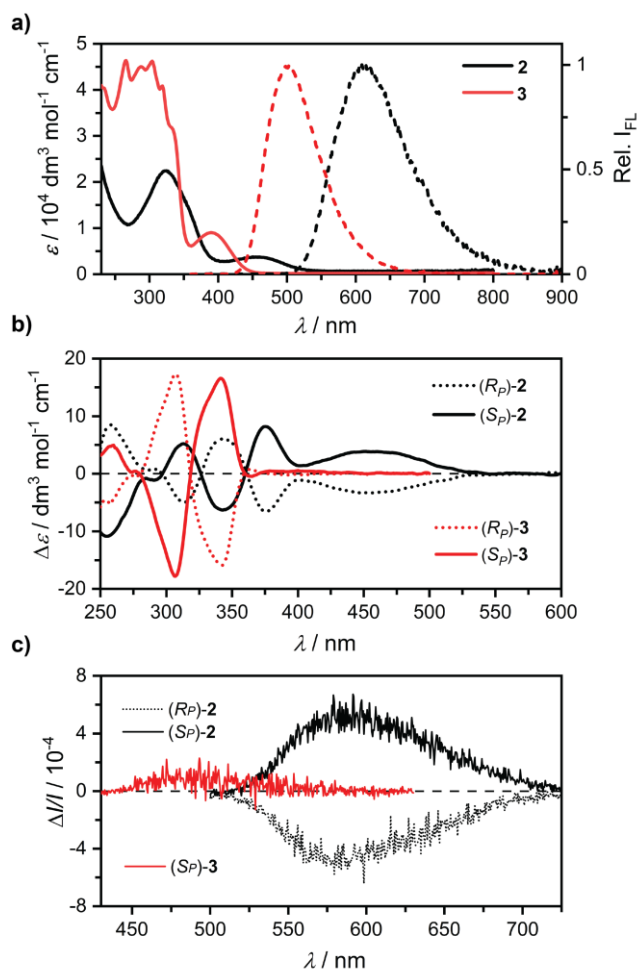


Figure 3.2. (a) UV-vis absorption (solid line) and fluorescence (dashed line) spectra of **2** and **3**. (b) ECD of **2** and **3** ($\Delta\epsilon$ of **3** scaled by 0.1) and (c) CPL spectra of **2** and **3**. All samples were measured in dichloromethane ($c \sim 5 \times 10^{-5} \text{ M}$).

The absorption of **2** is similar to that of $[n]$ CPPs with a characteristic $S_0 \rightarrow S_2$ transition at 324 nm, blue-shifted by 4 nm compared to **1**,³³ showing a minor influence of replacing a phenylene by BT on the dominant absorption maximum. Absorption profile of **3** at ~ 300 nm is not well-resolved due to the presence of multiple electronic transitions of similar energy (Table A3.2). The absorption band for the $S_0 \rightarrow S_1$ transition is observed for **2** and **3** at 450 nm ($\epsilon = 0.3 \times 10^4 \text{ M}^{-1}$

cm^{-1}) and 389 nm ($0.9 \times 10^4 \text{ M}^{-1} \text{ cm}^{-1}$), respectively. Both the bathochromic shift and the decrease in the ϵ with increased conjugation in **2** may suggest an enhancement of the charge-transfer character in this transition.

However, we observe only a minor and comparable solvatochromism in **2** and **3** (Figures A3.7–A3.8). Our TD-DFT calculations (Tables A3.1 and A3.2, Figure A3.18) confirm that the lowest-energy absorption in **2** corresponds to the HOMO→LUMO transition, while it is characterized by the HOMO–2→LUMO transition in **3**. The HOMO in **2** involves BT and all six phenylenes and the LUMO is centred mainly in the BT moiety, while both MOs are dominantly localised in the BT moiety with adjacent phenylenes in **3**. The MO analysis and the computed excited state dipole moments thus show marginal charge-transfer character in the lowest-energy transition in **2**, and the changes in the absorption can be attributed solely to the increase in conjugation. The same effect is also clearly visible upon comparison of the photoluminescence spectra (Figure 3.2a). Both macrocycles are strongly luminescent with the emission maxima at $\lambda_{\text{em}} \geq 500$ nm (Table 3.1). The maximum in **2** resides at impressive 609 nm with the band onset reaching to the near IR region (~ 850 nm) establishing this molecule as the most red-shifted chiral nano hoop reported to date with a good ϕ_{F} (see below).

Table 3.1. Summary of the photophysical properties.

Compound	λ_{abs} (nm)	λ_{em} (nm)	ϕ_{F}	ϵ^b ($10^4 \text{ M}^{-1} \text{ cm}^{-1}$)	$ g_{\text{abs}} ^c$ (10^{-3})	$ g_{\text{lum}} ^d$ (10^{-3})	Stokes shift (cm^{-1})	B_{CPL}^e ($\text{M}^{-1} \text{ cm}^{-1}$)
1 ^f	<400, 328	470	0.72	–, 3.95	$\sim 11^g$ (20.1 ^h)	2.7 (2.3 ^h)	– ⁱ	36.8
2	450, 324	609 (596 ^h)	0.48	0.3, 2.2	1.3 (1.2 ^h ; 0.27 ^h)	0.5 (0.7 ^h)	5800	0.36
3	389, ~ 320	500 (473 ^h)	0.70	0.9, 3.5	0.3 (0.22 ^h)	<0.1 (0.17 ^h)	5700	<0.3
BT[10]CPP ^k	445, 334	571	0.59	–, 5.4	–	–	4960	–

^aDichloromethane solutions at room temperature ($\sim 10^{-5}$ M). ^bThe values for the first and the second absorption maximum, respectively. ^cAt 450 and 390 nm for **2** and **3**, respectively. ^dAt 600 and 500 nm for **2** and **3**, respectively. ^eBrightness of CPL ($B_{\text{CPL}} = \epsilon \times \phi_{\text{F}} \times |g_{\text{lum}}|/2$). ^fFrom ref. 33. ^gEstimated for the $S_0 \rightarrow S_1$ transition from data in ref. 33. ^hTD-CAM-B3LYP/6-31g(d) value. ⁱValue cannot be determined because the $S_0 \rightarrow S_1$ transition is not resolved. ^jCalculated for a model **2'** with interrupted conjugation (see text and Figure 3.3). ^kFrom ref. 35.

In addition, macrocycle **3** itself represents the first chiral nano hoop precursor with bright green fluorescence at 500 nm. The red shift in **2** compared to **3** is 3580 cm^{-1} (109 nm) and can again, be attributed to the increase in the π -conjugation length. Interestingly, the Stokes shifts in **2** and **3** are

significant at 5800 cm^{-1} and 5700 cm^{-1} , respectively, yet comparable despite the different π -conjugation. Clearly, mostly the energy of the S_1 state but not the reorganization from the Franck-Condon point ($\Delta E_{2,3} \sim 100\text{ cm}^{-1}$) is affected by the extra conjugation. Both **2** and **3** display high ϕ_F of 0.48 and 0.70, respectively, despite the significant shift in the emission, particularly in **2**. Both nano hoops are also fluorescent in the solid state (Figure A3.9). Comparison of **2** and **1**, which has the same size, shows that the fluorescence maximum is red-shifted by striking 139 nm (4860 cm^{-1}). Clearly, incorporation of BT into carbon nano hoops proposed by Jasti³⁵ is a very effective strategy to achieve a significant red-shift. The λ_{em} in **2** is even red-shifted by 38 nm compared to BT[10]CPP without a notable drop in ϕ_F .

Chiroptical properties and theoretical calculations: The three compounds, **1**, **2**, and **3**, form a series that shares the same critical structural features (Figure 3.1): (i) a PCP unit with planar chirality, (ii) a central phenylene or BT unit attached to PCP via (iii) two arms with three *p*-phenylenes each, although masked as cyclohexa-2,5-dienyls in **3**. Nevertheless, these chiral compounds have similar size, geometry, and are all luminescent (Table 3.1). This provided us with a rare opportunity to use their chiroptical properties to systematically investigate the effect of exciton delocalization on the chiroptical properties of these PCP-based nano hoops. To tackle the proposed challenge, we successfully separated the enantiomers of **2** and **3** using recycling HPLC equipped with a chiral stationary phase (Figure A3.10–A3.11). We characterized the individual enantiomers by ECD and CPL (Figure 3.2b–c, Table 3.1, Figures A3.12–A3.15). We fully assigned the recorded ECD and CPL spectra to each individual enantiomer by TD-DFT calculations (Figures A3.16–A3.17). The observed CPL response for the isolated enantiomer of **3** was very weak, reaching the detection limit of our instrument. Nevertheless, the obtained experimental and calculated values of g_{abs} and g_{lum} agree well for both **2** and **3**. Both factors for **1** can be derived from data in ref. 33 and we additionally calculated them at the same level of theory as for **2** and **3** (Table A3.5–A3.6).

The measured dissymmetry factors for **2** and **3** are markedly lower compared to those obtained for **1**, and obey the following trend: $g_{abs,lum}(\mathbf{1}) > g_{abs,lum}(\mathbf{2}) > g_{abs,lum}(\mathbf{3})$. The mutual differences in the series reach roughly an order of magnitude and so decreases the B_{CPL} . To allow for a balanced comparison between the three compounds, we examined the individual lowest-energy transitions by computing the corresponding natural transition orbitals (NTOs, Figure A3.18, A3.19) and electronic transition densities (Figure 3.3).

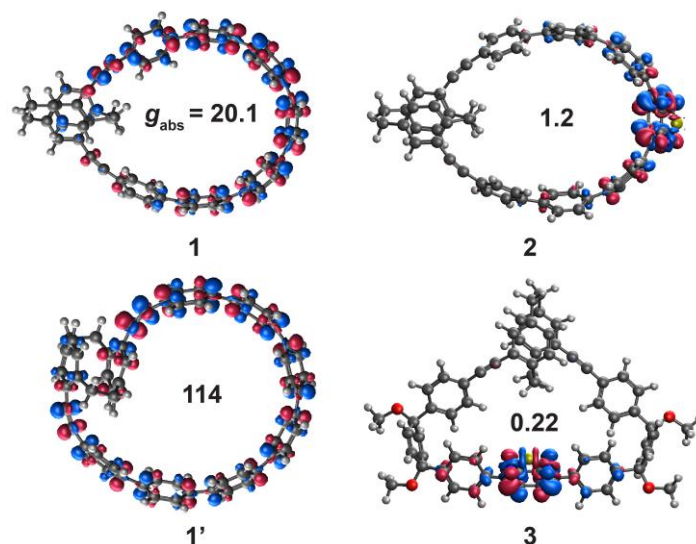


Figure 3.3. The $S_0 \rightarrow S_1$ transition densities and g_{abs} values ($\times 10^3$) calculated for **1**, **1'**, **2**, **3** and (TD-CAM-B3LYP/6-31g(d)), isosurface value = 0.004). See the appendix for the involved natural transition orbitals.

Inspection of the $S_0 \rightarrow S_1$ transition densities and NTOs shows that the exciton in **1** reaches the PCP unit in the nanohoop and mixes some of its MOs. The situation changes in **2**, where both the occupied and virtual NTOs are localized to the half of the nanohoop with the BT unit. Clearly, replacing a *p*-phenylene for a strong electron acceptor, such as BT, localizes the electron and the hole density away from the PCP unit upon excitation. The turn-off of the conjugation in **3** further exacerbates the effect. The same observation can be made for the $S_1 \rightarrow S_0$ transition (Figures A3.20), reflecting the trend in the CPL response, although the effect is more subtle as the result of exciton localization upon relaxation from the Franck-Condon point (see below).

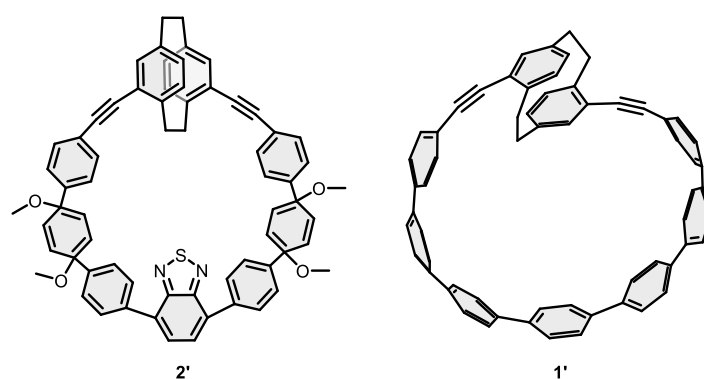


Figure 3.4. Structure of **2'** and **1'**

To fully exclude that the observed outcome emerged from the change in the geometry, such as between **2** and **3**, where the rehybridization in the latter does affect the PCP and BT distance and

orientation (Figure 3.3), we designed a model compound **2'** (Figure 3.4) for a computational experiment to effectively turn off the conjugation in **2**. This was achieved by addition of four methoxy groups to the central *p*-phenylenes as in **3** and relaxing their coordinates, while keeping all others frozen in the process. As a result, the distance and orientation of BT and PCP in **2'** remained identical to those in **2** (Figure A3.21). The partial rehybridization of the central *p*-phenylenes in our computational model had a dramatic effect on the NTOs involved in the $S_0 \rightarrow S_1$ transition (**2'**, Figure A3.22). The partially delocalized NTOs in **2** collapsed to localized NTOs similar in shape to those in **3**. Essentially, the nature of the transition in **2'** became the same as in **3** despite the minimal effect on the PCP and BT geometry found in **2**. Accordingly, the calculated g_{abs} dropped to a value commensurate to that found for **3**.

Clearly, the lack of conjugation that allows the exciton to couple BT and the PCP, has a detrimental effect on the size of the dissymmetry factor. Nevertheless, the values of g_{abs} and g_{lum} in all three compounds are relatively small and even those in **1** do not exceed the values of typical small organic chromophores. We argue that the reason is the connection of PCP to the remainder chromophore via the *pseudo-meta* positions, which do not permit an effective exciton delocalization to the chiral unit according to the structure–property relationship that we constructed here. We thus decided to test its predictive ability and examine if using a *pseudo-para* instead of *pseudo-meta* PCP in **1** could provide a chiral carbon nanochoop³⁷ (**1'**, Figure 3.3 and Figure 3.4) with a larger exciton delocalization and, therefore, a larger dissymmetry factor. The internal area of this model analogue would also be slightly enhanced compared to **1**, affecting $|m|$ and subsequently g_{abs} . We calculated the parameters of the $S_0 \rightarrow S_1$ transition in hypothetical enantiomer **1'** and investigated the corresponding transition density and NTOs (Figure 3.3, Figure A3.22, Table A3.5). Indeed, the individual MOs of pseudo-para PCP are now mixed with those from the curved para-phenylenes and the PCP is thus strongly involved in the transition. The predicted dissymmetry factor for **1'** reached a value of $|g_{\text{abs}}| = 0.114$, an order of magnitude higher than that in **1**. Note that this is an extraordinary g_{abs} for a molecule that lacks any symmetry. Comparable values of g_{abs} are typically achieved in macrocycles that belong to high symmetry point groups.^{9,35,36}

Extending the delocalization directly affects the value of the angle (θ) between μ and m , which is nearly 90° in **3** (Figure A3.23–A3.24, Table A3.4) and increases steadily in the series to a value of 110° in **1'** (Tables A3.3–A3.6). Despite the transition density that spans the entire **1'**, the $|\cos(\theta)| = 0.342$ highlights the importance of approaching a uniform exciton delocalization that could be reached for chromophores with D_n symmetry.^{11,38} Adopting such high symmetry is, however, beyond reach for carbon nanochoops with a single chiral element. An alternative strategy that

provides a higher flexibility in molecular design with a slight sacrifice in the g_{abs} factor is imposing structures to a C_n point group of symmetry,³⁸ in which the individual components of μ and m transform under the same irreducible representations, *i.e.*, they can even be parallel. Lifting the symmetry further could still lead to acceptable values of θ ($\geq 135^\circ$) if the exciton was sufficiently delocalized. Similar trend is observed for $|m|$ that is slightly enhanced in **1'** because of an extended exciton delocalization, which would ultimately be related to the slight increase in the internal area of the helical circuit.

However, excited state reorganization in carbon nanohoops is known to lead to exciton localization,^{39,40} which often decreases θ close to 90° compromising the value of g_{lum} in CPL similarly to what we observe in the compounds investigated here. Preventing exciton localization is challenging, particularly in carbon nanohoops that undergo extensive excited state geometry relaxation. For this reason, bright chiral fluorophores with or close to C_2 symmetry and small Stokes shifts could preserve sufficiently delocalized excited states in non-polar environments, representing interesting targets to accomplish CPL materials with high B_{CPL} .

3.3 Conclusion

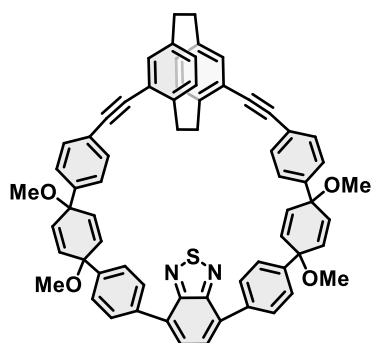
In summary, we synthesized two macrocycles incorporating planar chiral *pseudo-meta* [2.2]paracyclophane and benzothiadiazole that allowed for a significant red-shift of their CPL, while displaying high fluorescence quantum yields and large Stokes shifts. These molecules allowed for unprecedented, systematic investigation of the role of exciton delocalization on the chiroptical properties in carbon nanohoops. Thereby, we constructed a unique structure–property relationship that allowed for a critical insight into the factors limiting the desired chiroptical response. We believe that this work will thus aid and abet the development of robust guidelines to design materials with strong electronic circular dichroism or circularly polarized luminescence with high brightness.

3.4 Appendix

General remarks: Additional material that can be found in the Supporting Information of the published paper (<https://doi.org/10.1039/D4SC07333A>): General experimental details, 2D NMRs, quantum yield determination plots, FMOs of all compounds, DFT parameters tables for **1** and **1'**, HPLC chromatograms of individual enantiomers, cartesian coordinates.

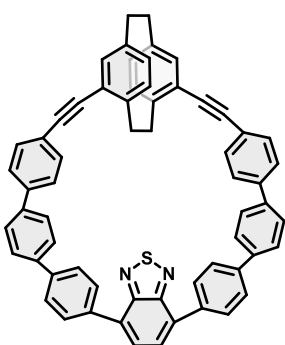
Compounds **4-6** were synthesized following the literature protocols.^{33,41} Spectral data matched the values reported in the literature. Compound **7** is commercially available.

Synthesis of **3**:



To a 500 ml round-bottom flask, **6** (153 mg, 0.154 mmol, 1 equiv), **7** (63 mg, 0.161 mmol, 1.05 equiv) and SPhos Pd Gen 3 (12 mg, 0.015 mmol, 0.1 equiv) were added. The flask was evacuated and backfilled with argon five times. 1,4-dioxane and 2 M aq K_3PO_4 solution were sparged with Ar for 2 hours prior to use. To the reaction mixture, dioxane (200 ml) was added and the solution was sparged with Ar for another 1 hour. The reaction mixture was heated to 80 °C at which point the degassed K_3PO_4 solution (20 ml) was added dropwise. The reaction mixture was allowed to stir overnight at 80 °C. The solution was cooled down and filtered through celite and the flask was rinsed using ethyl acetate. The filtrate was washed with brine, dried over sodium sulfate and volatiles were removed under reduced pressure. The product was purified using silica gel chromatography (30% ethyl acetate in petroleum ether) and gel permeation chromatography (chloroform) to afford the product **4** as a green crystalline solid (34 mg, 23%). **¹H NMR** (400 MHz, $CDCl_3$, 298 K, δ /ppm): 7.97 (d, J = 8.5 Hz, 4H), 7.84 (s, 2H), 7.56 (d, J = 8.4 Hz, 4H), 7.38 (d, J = 8.5 Hz, 4H), 7.24 (d, J = 8.3 Hz, 4H), 6.91 (d, J = 7.9 Hz, 2H), 6.59 (d, J = 1.8 Hz, 2H), 6.47 (dd, J = 7.9, 1.8 Hz, 2H), 6.33 (ddd, J = 10.4, 3.8, 2.4 Hz, 4H), 6.18 – 6.06 (m, 4H), 3.54 (m, 2H), 3.51 (s, 6H), 3.48 (s, 6H), 3.23 – 3.10 (m, 2H), 3.08 – 2.96 (m, 2H), 2.93 – 2.79 (m, 2H). **¹³C NMR** (101 MHz, $CDCl_3$, 298 K, δ /ppm): 154.25, 142.78, 142.67, 139.56, 137.01, 135.80, 134.30, 134.22, 133.15, 132.93, 132.84, 132.18, 131.16, 131.05, 129.43, 128.35, 126.72, 126.32, 124.94, 122.98, 93.16, 89.81, 75.50, 75.26, 52.25, 52.06, 35.03, 33.48, 29.72. **HRMS** (FD+): m/z calculated for $C_{66}H_{52}N_2O_4S$: 968.3648, found 968.3645.

Synthesis of **2**:



Method 1: An H_2SnCl_4 solution was freshly prepared: $SnCl_2 \cdot 2H_2O$ (147 mg, 138 μ mol) was suspended in THF (5 mL) and 37% aqueous HCl (100 μ L) was added and the resulting mixture was stirred for 30 min. To a 50 ml round bottom flask, **3** (7 mg, 0.007 mmol, 1 equiv) was dissolved in 7 ml THF and H_2SnCl_4 solution (2 ml, 0.21 mmol, 0.122 M, 30 equiv) was added dropwise. The fluorescence of the solution changes from bright green to bright yellow. After completion of the reaction, the reaction mixture was quenched with 2M aqueous NaOH solution. The aqueous layer was extracted with dichloromethane and organic layers

were combined and dried over sodium sulfate. The crude mixture was purified by column chromatography (SiO₂, 100% toluene) followed by gel permeation chromatography (Chloroform) to get an orange solid (3 mg, 60%). **Method 2:** A 1 M sodium naphthalide solution was freshly prepared: naphthalene (473 mg, 3.8 mmol) was added in 3.8 ml of THF. To this, sodium (125 mg, 5.56 mmol) was added under argon, and this was allowed to stir for 18 h. A dark green solution (sodium naphthalide, 1 M) is formed. To a 50 ml round bottom flask, **3** (6 mg, 0.006 mmol) was dissolved in 4 ml THF and was cooled to -78 °C and sodium naphthalide solution (0.4 ml, 1 M, 60 equiv) was added dropwise at this temperature. This was allowed to stir for 10 min before quenching it with 1 M solution of iodine in THF followed by sodium thiosulfate solution. The reaction mixture was extracted using dichloromethane and organic layers were combined and dried over sodium sulfate. The solvents were removed under reduced pressure. The crude mixture was purified by column chromatography (SiO₂, 100% toluene) followed by gel permeation chromatography (Chloroform) to get an orange solid (3.5 mg, 70%).

¹H NMR: ¹H NMR (400 MHz, CDCl₃, 298 K, δ/ppm): 7.99 (d, *J* = 8.5 Hz, 4H), 7.67 – 7.45 (m, 22H), 6.93 (d, *J* = 7.8 Hz, 2H), 6.54 (d, *J* = 1.8 Hz, 2H), 6.50 (dd, *J* = 7.8, 1.8 Hz, 2H), 3.34 – 3.21 (m, 2H), 3.19 – 3.04 (m, 2H), 2.90 – 2.71 (m, 4H). **¹³C NMR** (101 MHz, CDCl₃, 298 K, δ/ppm): δ 154.82, 145.03, 140.37, 139.82, 139.47, 138.68, 138.60, 136.41, 133.84, 132.42, 131.79, 131.67, 131.57, 130.61, 127.97, 127.72, 127.42, 127.35, 127.25, 124.62, 122.64, 94.71, 92.99, 35.47, 33.51. (The nano hoop sample was kept at high vacuum for 8 h, however the solvent peaks could still not be removed leading to the visible signals in up field region of the spectrum, therefore, only the chemical shifts for the signals that belong to the compound are mentioned here) **HRMS** (FD+): calculated for C₆₂H₄₀N₂S: 844.2912, found 844.2921.

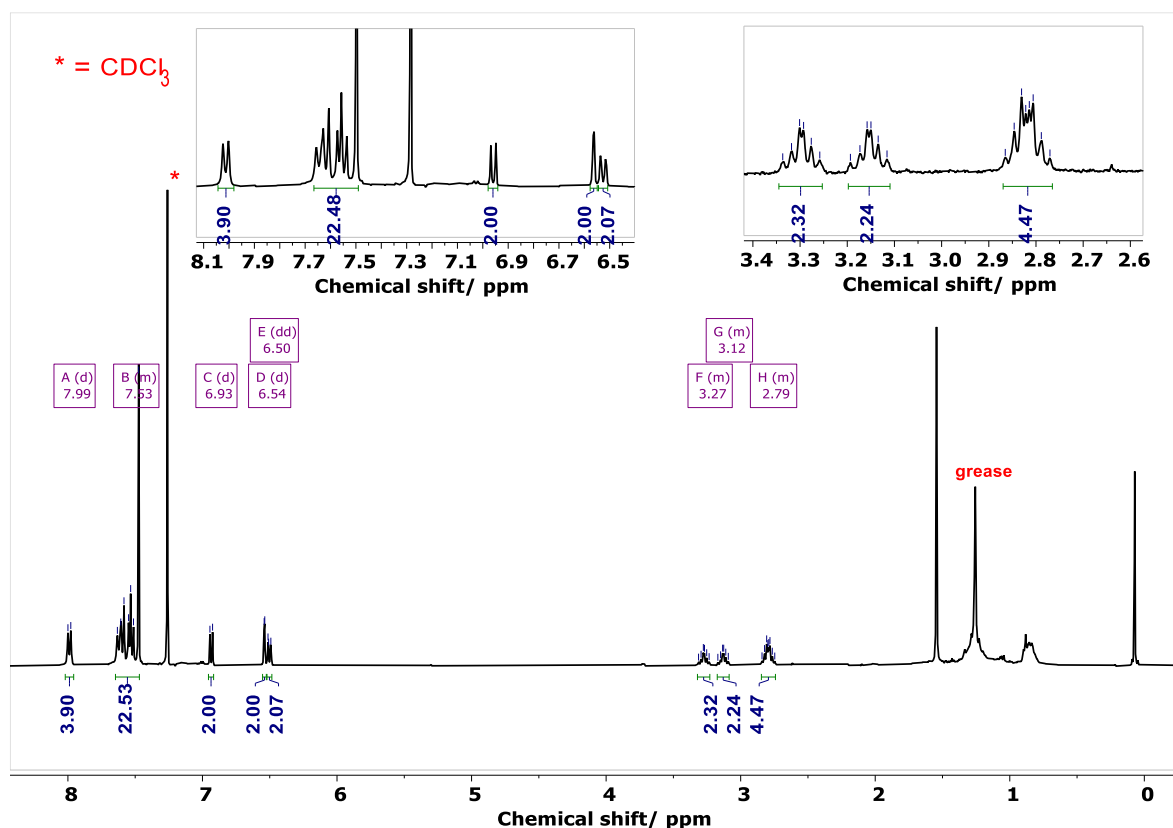
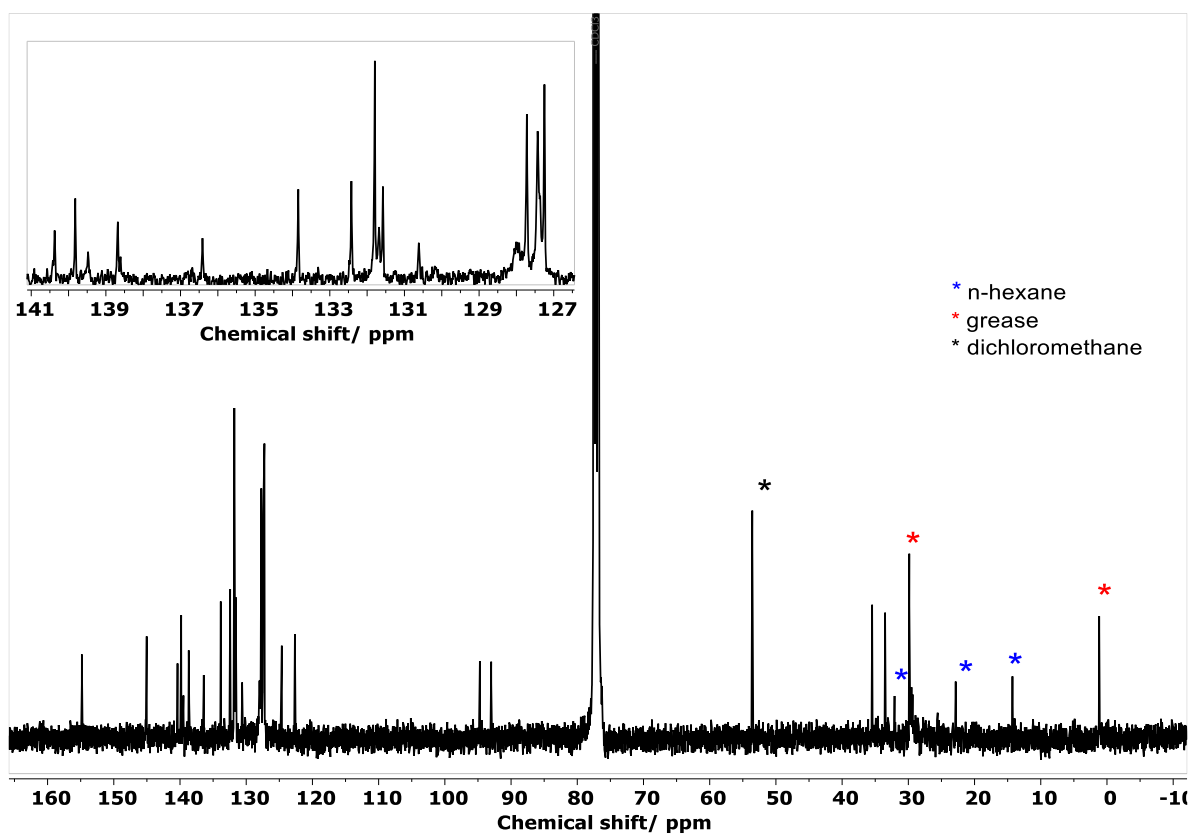
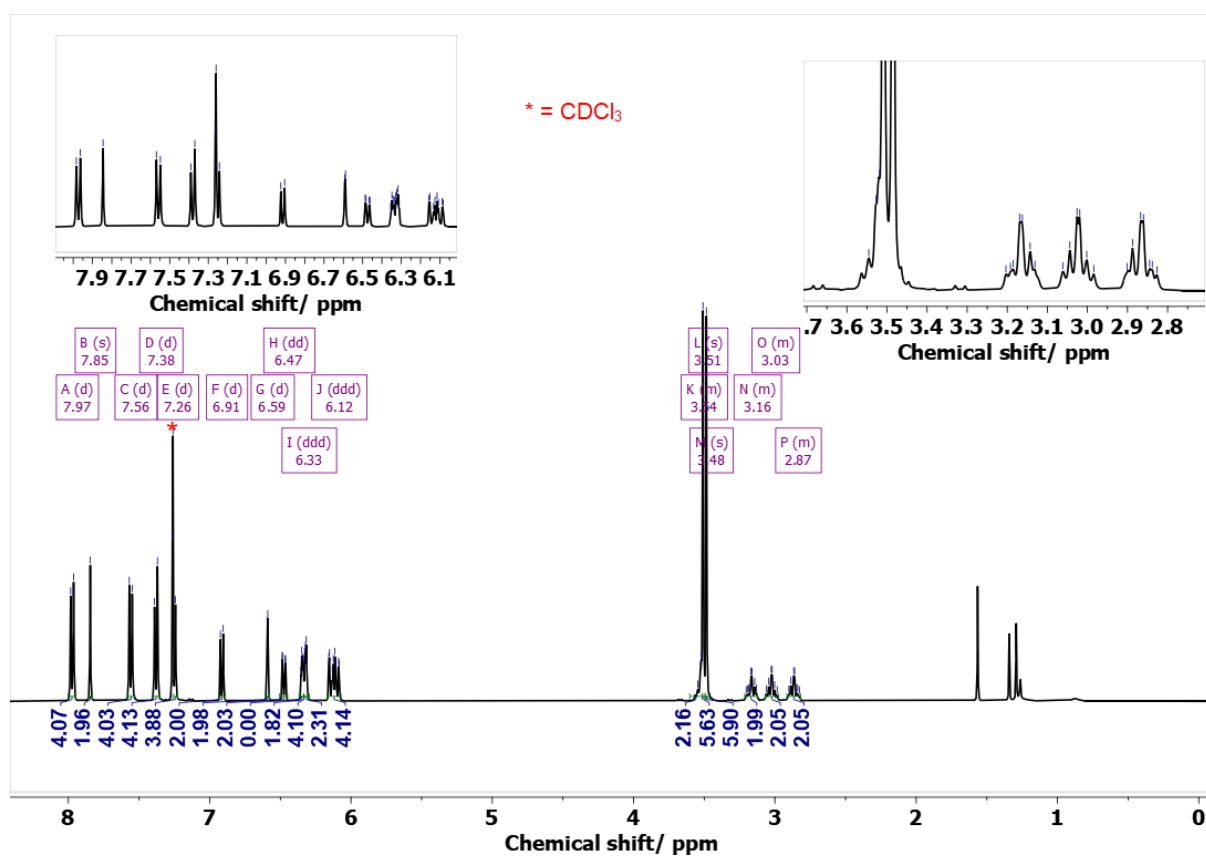


Figure A3.1. ¹H NMR spectrum of compound **2** in CDCl₃ recorded at 298 K.

Figure A3.2. ^{13}C NMR spectrum of compound 2 in CDCl_3 recorded at 298 K.Figure A3.3. ^1H NMR spectrum of compound 3 in CDCl_3 recorded at 298 K.

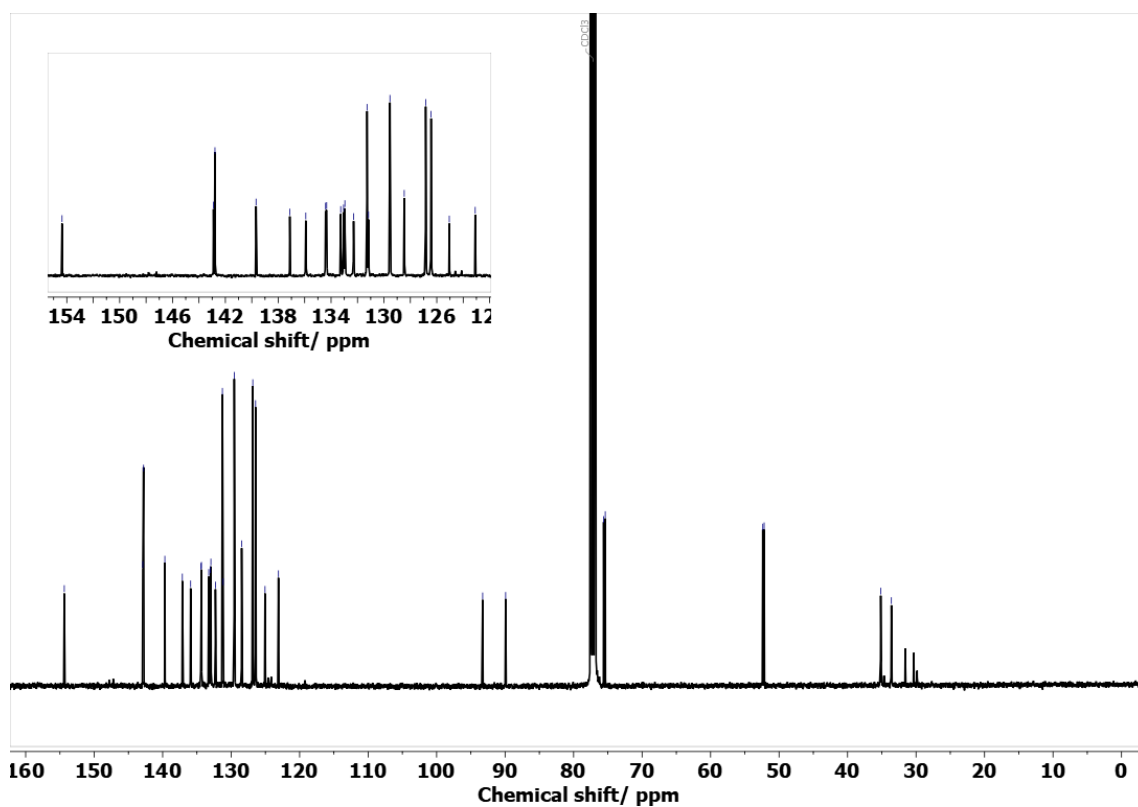


Figure A3.4. ^{13}C NMR spectrum of compound 3 in CDCl_3 recorded at 298 K.

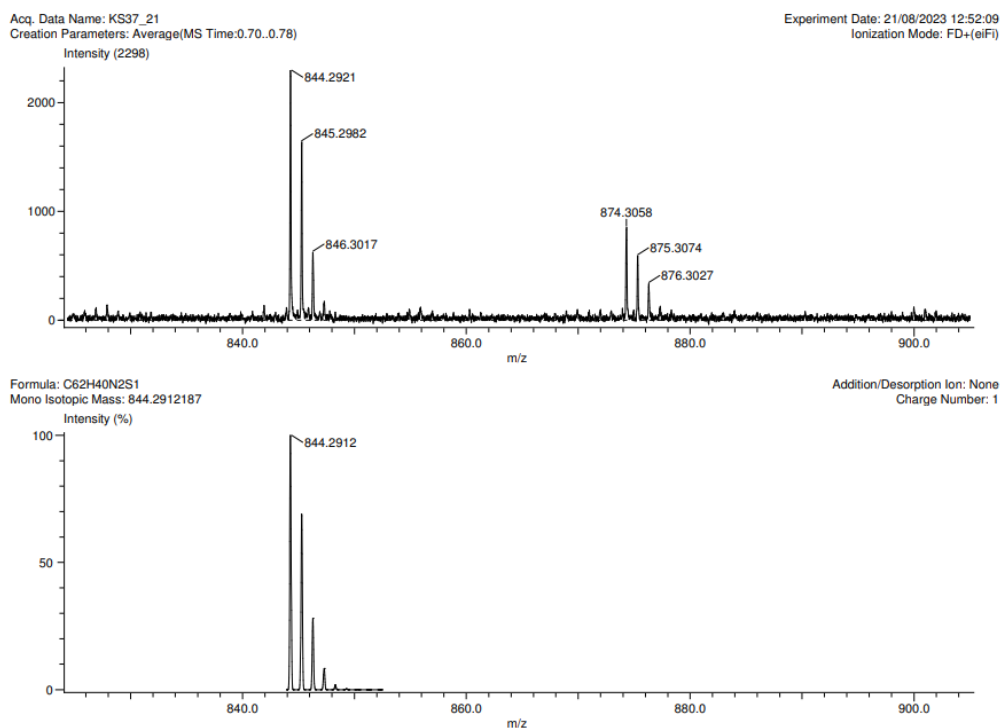


Figure A3.5. HRMS for compound 2.

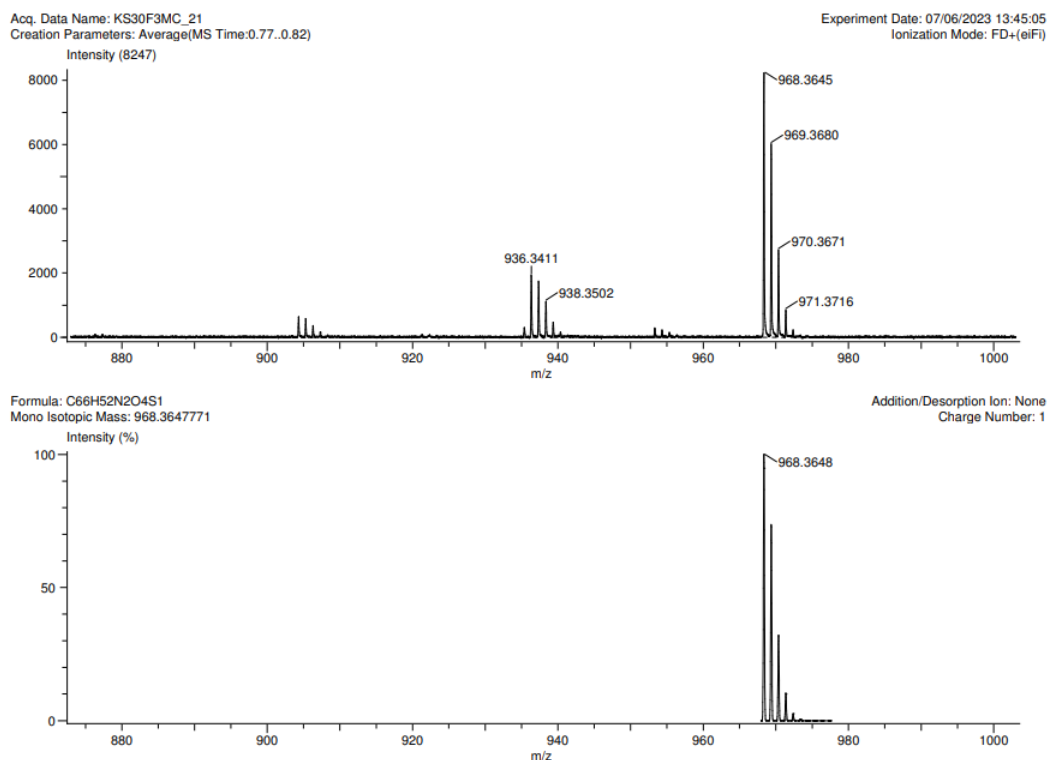


Figure A3.6. HRMS for compound **3**.

Photophysical Properties: We measured the photophysical properties of **2** and **3**. Excitation wavelength for all fluorescence measurements was 350 nm. Luminescence quantum yield of **2** (0.48) and **3** (0.70) was measured in dichloromethane using a relative quantum yield measurement method. [10]CPP in THF was used as a standard ($QY = 0.46$).¹⁹

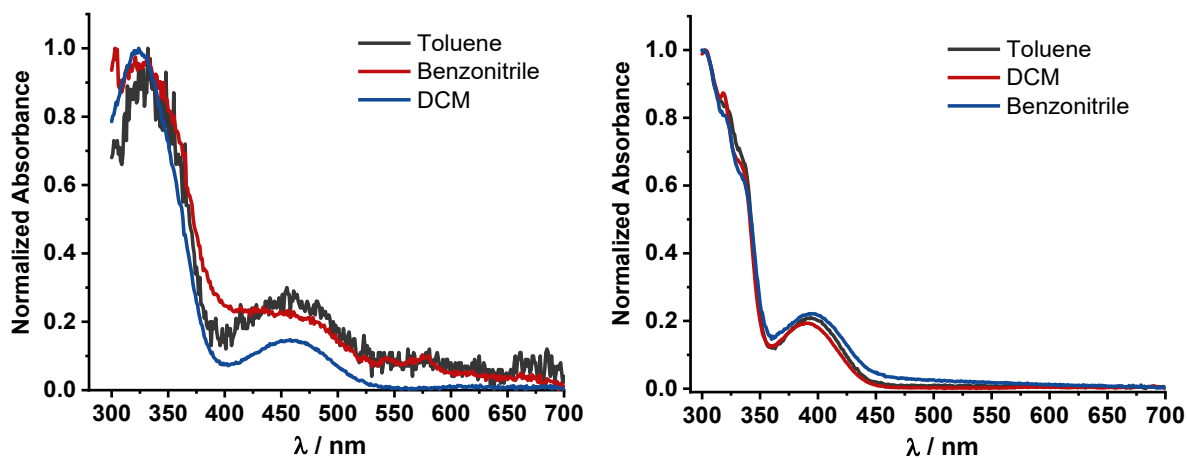


Figure A3.7. Normalized absorption spectra of **2** (left) and **3** (right) in different solvents.

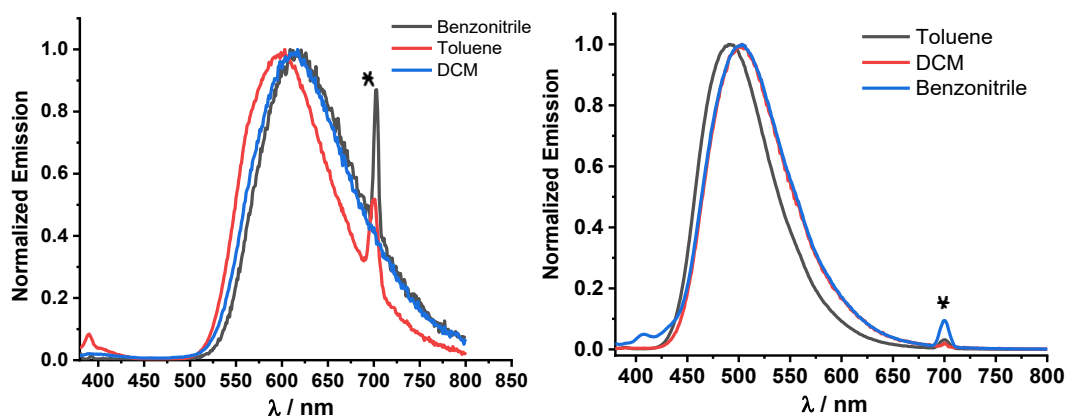


Figure A3.8. Normalized emission spectra of **2** (left) and **3** (right) in different solvents ($\lambda_{\text{exc}} = 350 \text{ nm}$) *= scattered light.



Figure A3.9. The solid-state fluorescence of **2** (left) and **3** (right).

Chiral HPLC: Enantiomers of **2** and **3** were resolved on a preparative scale using recycling HPLC equipped with a Chiralpak IG (20x250mm) column by Daicel. For **2**, 50% DCM in *n*-heptane was used as an eluent at 20 mL min^{-1} flow rate. For **3**, toluene/TBME/*n*-heptane (v/v, 1:7:2) was used as an eluent at 15 mL min^{-1} flow rate. Due to poor enantiomer separation for **3** (Figure A3.10), both enantiomers were individually reinjected after the 1st run (Figure A3.11).

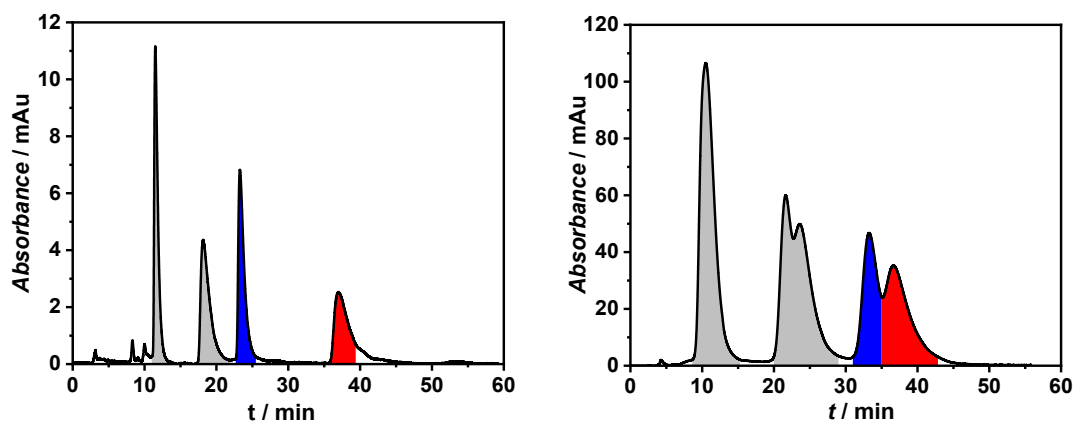


Figure A3.10. HPLC chromatogram of **2** (left) and **3** (right). A racemate was injected and recycled (grey) until peak separation. Enantiomer 1 (blue) and enantiomer 2 (red) of **2** (left) were collected in the 2nd cycle and correspond to (*S_p*)- and (*R_p*)-enantiomers, respectively. Enantiomer 1 (red) and enantiomer 2 (blue) of **3** (right) were collected in the 3rd cycle and correspond to (*R_p*)- and (*S_p*)-enantiomers, respectively.

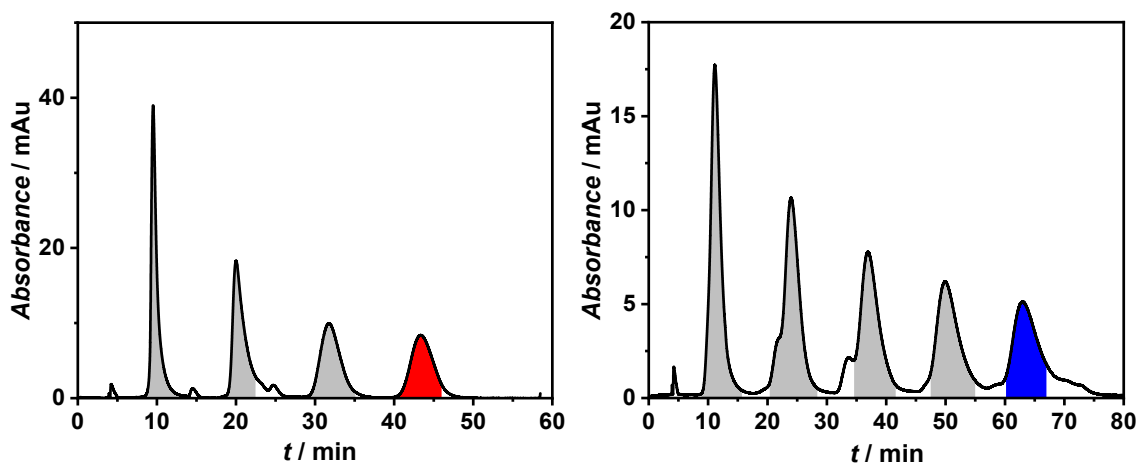


Figure A3.11. HPLC chromatogram of enantiomer 1 reinjection for **3** (left). The peak was recycled (grey) for 3 times before collection (red) and corresponds to (*R_p*)-enantiomer. The sample was then reinjected to analytical HPLC to confirm its purity. HPLC chromatogram of enantiomer 2 reinjection for **3** (right). The peak was recycled (grey) for 4 times before collection (blue) and corresponds to (*S_p*)-enantiomer. Two fractions of the blue region were collected, the second when the UV intensity reached the maximum to ensure the enantiomeric purity of the sample.

Chiroptical Properties: Circular dichroism (CD) and circularly polarized luminescence (CPL) spectra of **2** and **3** were measured in dichloromethane. CPL signal of **3** was too weak to measure spectra of higher quality as it was close to detection limit of the instrument.

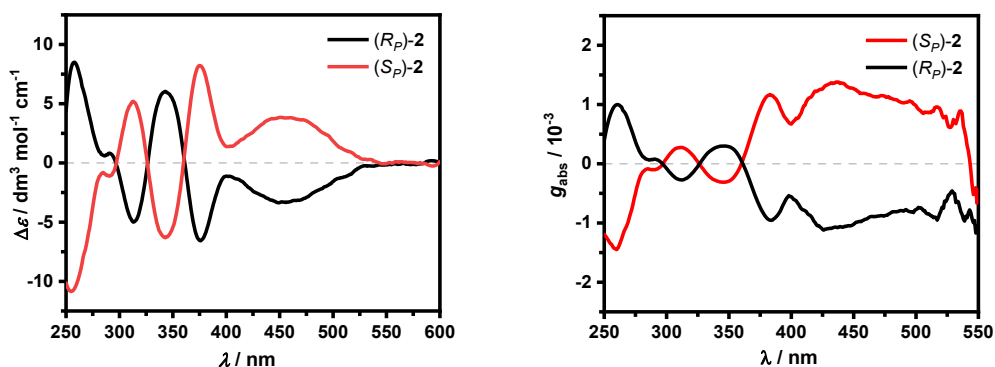


Figure A3.12. CD spectra (left) and g_{abs} plot (right) of **2**.

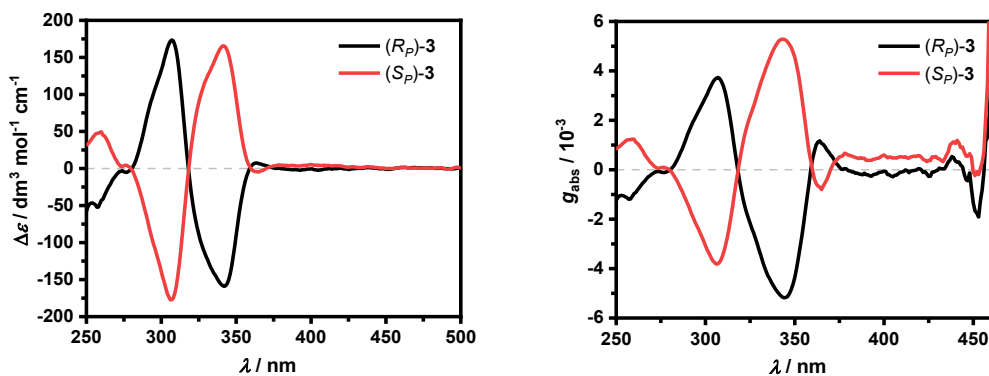


Figure A3.13. CD spectra (left) and g_{abs} plot (right) of **3**.

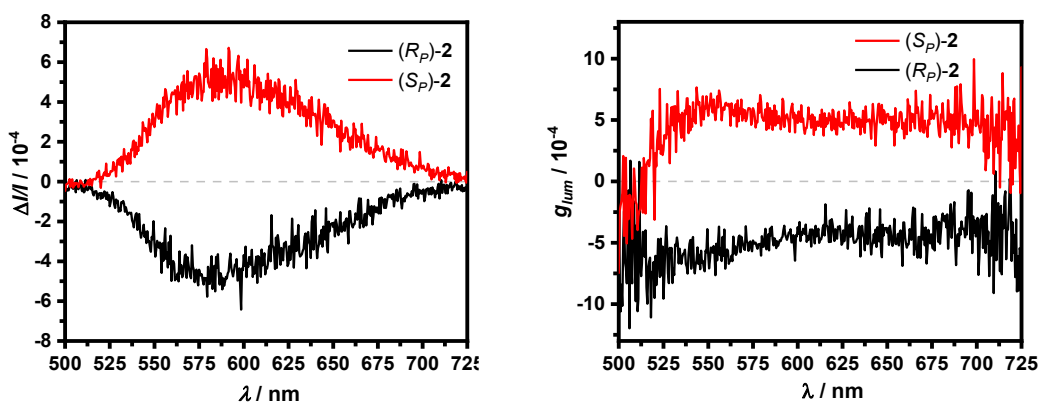


Figure A3.14. CPL spectra (left) and g_{lum} plot (right) of **2**.

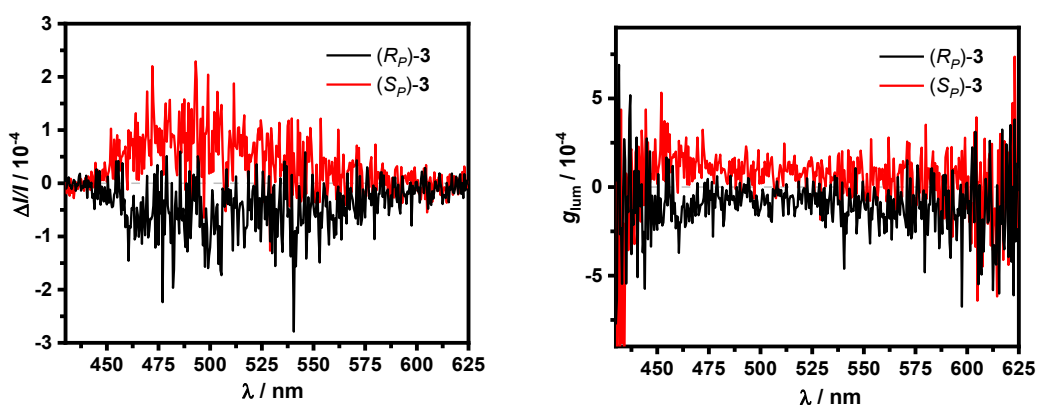


Figure A3.15. CPL spectra (left) and g_{lum} plot (right) of **3**.

DFT Calculations: Calculations were performed with Gaussian 09⁴² (release D.01) software. The geometries of the potential energy surface minima were optimized at D3-B3LYP/6-31g(d) level of theory. In a subsequent frequency calculation, all of the vibrational frequencies were real, confirming the character of found stationary points as minima. UltraFine integration grid was used in all calculations. CAM-B3LYP/6-31g(d) was used for time dependent calculations and to optimize the geometries of the excited states. To simulate CD spectra, first 10 transitions were calculated. Empirical vibrational broadening of 0.3 and 0.2 eV was used for **2** and **3**, respectively, and the calculated spectra were shifted by -0.2 eV for both. The velocity form of the rotatory strength was used.

Table A3.1. Electronic transitions and their respective energies (E), wavelengths (λ), oscillator strengths (f) and orbital contributions for **2**.

Transition	E / eV	λ / nm	f	Orbital contributions ^a
1	2.9181	424.88	0.3393	HOMO→LUMO (82%)
2	3.9212	316.19	0.0266	HOMO→LUMO+1 (44%) HOMO-1→LUMO+2 (16%)
3	3.9484	314.01	1.2119	HOMO-1→LUMO (48%) HOMO-3→LUMO (16%) HOMO-6→LUMO (12%)
4	4.2212	293.72	0.5349	HOMO-1→LUMO+1 (25%) HOMO-3→LUMO+3 (14%) HOMO→LUMO+2 (12%)
5	4.3199	287.01	0.5691	HOMO-2→LUMO+1 (18%) HOMO→LUMO+2 (13%)

^aOnly the contributions larger than 10% are listed.

Table A3.2. Electronic transitions and their respective energies (E), wavelengths (λ), oscillator strengths (f) and orbital contributions for **3**.

Transition	E / eV	λ / nm	f	Orbital contributions ^a
1	3.3321	372.09	0.3268	HOMO-2→LUMO (94%)
2	3.9473	314.1	0.9212	HOMO→LUMO+1 (74%) HOMO-1→LUMO+2 (16%)
3	4.079	303.96	0.3218	HOMO-1→LUMO+1 (73%)
4	4.2262	293.37	0.0012	HOMO→LUMO (86%) HOMO-1→LUMO (12%)
5	4.3545	284.73	0.3258	HOMO→LUMO+2 (45%) HOMO-3→LUMO+1 (19%)

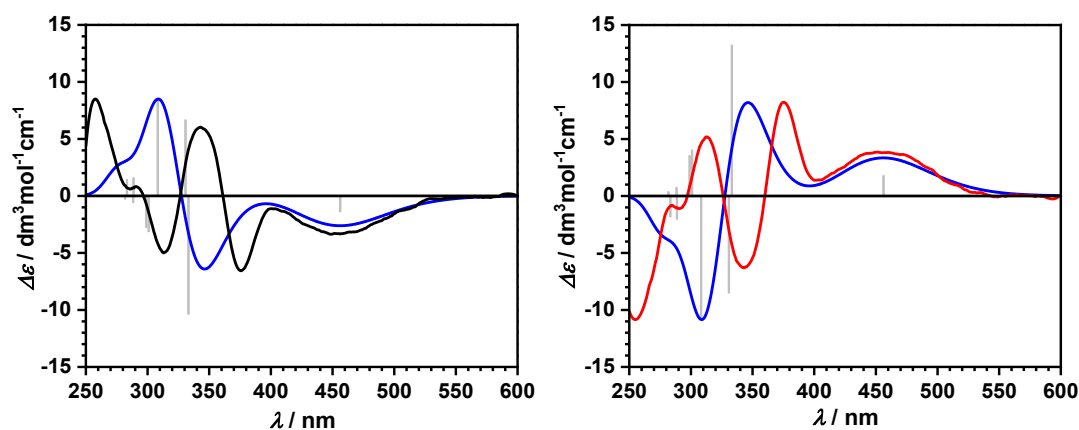
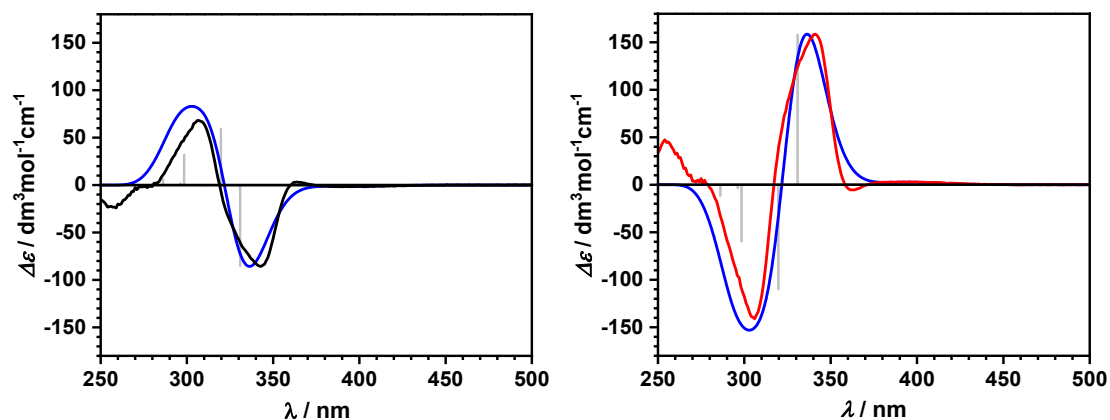
^aOnly the contributions larger than 10% are listed.**Figure A3.16.** Experimental (black) and calculated (blue) CD spectra of (R_p)-**2** (left) with excitation transitions (grey lines). Experimental (red) and calculated (blue) CD spectra of (S_p)-**2** (right) with excitation transitions (grey lines).**Figure A3.17.** Experimental (black) and calculated (blue) CD spectra of (R_p)-**3** (left) with excitation transitions (grey lines). Experimental (red) and calculated (blue) CD spectra of (S_p)-**3** (right) with excitation transitions (grey lines).

Table A3.3. Calculated energies (E), oscillator strengths (f), electric (μ) and magnetic (m) transition dipole moments, and angles (θ) between them, rotatory strengths (R , velocity form), dipole strengths (D) and calculated dissymmetry factor (g_{abs}) values for ground state geometries.

Compound (Transition)	E / eV	f	$ \mu / 10^{-18} \text{ esu}\cdot\text{cm}$	$ m / 10^{-20} \text{ erg}\cdot\text{G}^{-1}$	$\theta / ^\circ$	$R / 10^{-40} \text{ esu erg cm G}^{-1}$	$D / 10^{-36} \text{ esu}^2 \text{ cm}^2 \text{ erg}^2 \text{ G}^{-2}$	$g_{abs} / 10^{-3}$
R_{P-2} ($S_0 - S_1$)	2.9181	0.3393	5.54	5.78	91.69	-95.6253	30.66	-1.25
R_{P-2} ($S_0 - S_2$)	3.9212	0.0266	1.34	9.29	126.52	-746.8473	1.80	-166.24
R_{P-3} ($S_0 - S_1$)	3.3321	0.3268	5.09	3.69	90.44	-14.3600	25.87	-0.22
R_{P-3} ($S_0 - S_2$)	3.9473	0.9212	7.84	6.27	102.88	-1075.3783	61.55	-6.99

Table A3.4. Calculated energies (E), oscillator strengths (f), electric (μ) and magnetic (m) transition dipole moments, and angles (θ) between them, rotatory strengths (R , velocity form), dipole strengths (D) and calculated dissymmetry factor (g_{lum}) values for 1st excited state geometries.

Compound (Transition)	E / eV	f	$ \mu / 10^{-18} \text{ esu}\cdot\text{cm}$	$ m / 10^{-20} \text{ erg}\cdot\text{G}^{-1}$	$\theta / ^\circ$	$R / 10^{-40} \text{ esu erg cm G}^{-1}$	$D / 10^{-36} \text{ esu}^2 \text{ cm}^2 \text{ erg}^2 \text{ G}^{-2}$	$g_{lum} / 10^{-3}$
R_{P-2} ($S_1 - S_0$)	2.0811	0.3787	6.93	4.78	91.39	-82.9015	47.98	-0.69
R_{P-3} ($S_1 - S_0$)	2.6229	0.4367	6.63	3.20	90.49	-18.3871	43.91	-0.17

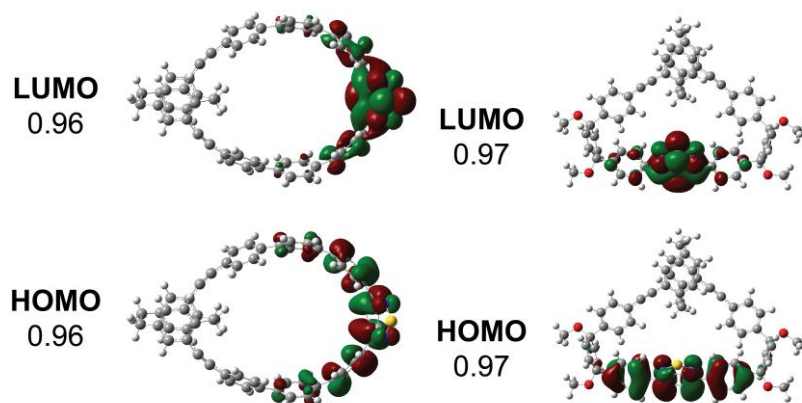


Figure A3.18. Natural transition orbitals and occupancies of the $S_0 \rightarrow S_1$ transition in **2** (left) and **3** (right).

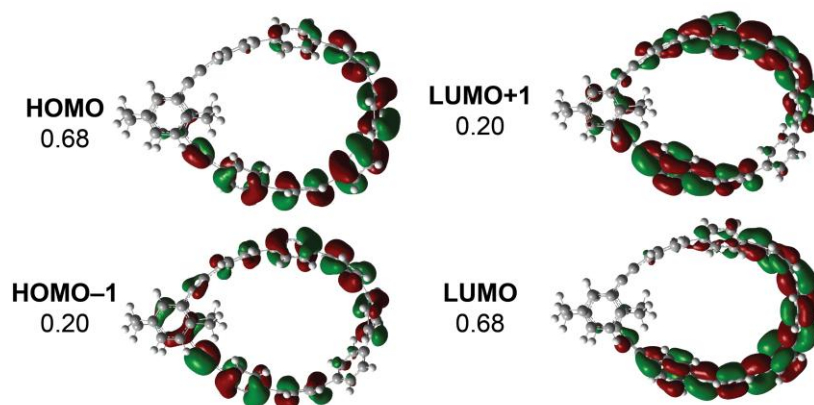


Figure A3.19. Natural transition orbitals and occupancies of the $S_0 \rightarrow S_1$ transition in **1**.

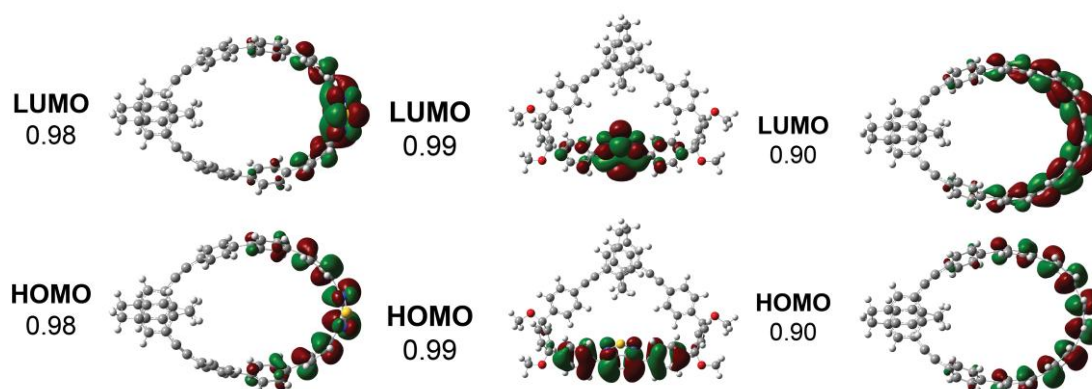


Figure A3.20. Natural transition orbitals and occupancies of the $S_1 \rightarrow S_0$ transition in **2** (left) and **3** (middle) and **1** (right).

The structure of **2** was modified with methoxy groups and the resulting structure **2'** was optimized at D3-B3LYP/6-31g(d) level of theory with the coordinates of all atoms frozen except of the cyclohexadiene moieties and added methoxy groups (Figure A3.21).

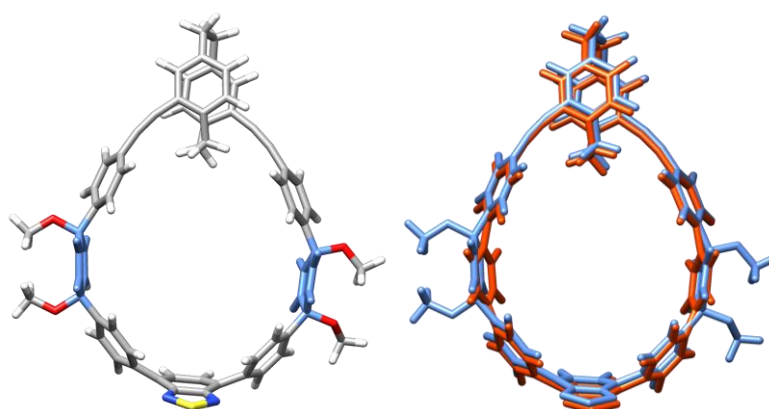


Figure A3.21. The optimized structure of **2'** with the optimized atoms marked in blue (left) and overlay (right) of the structures of **2** (orange) and **2'** (blue).

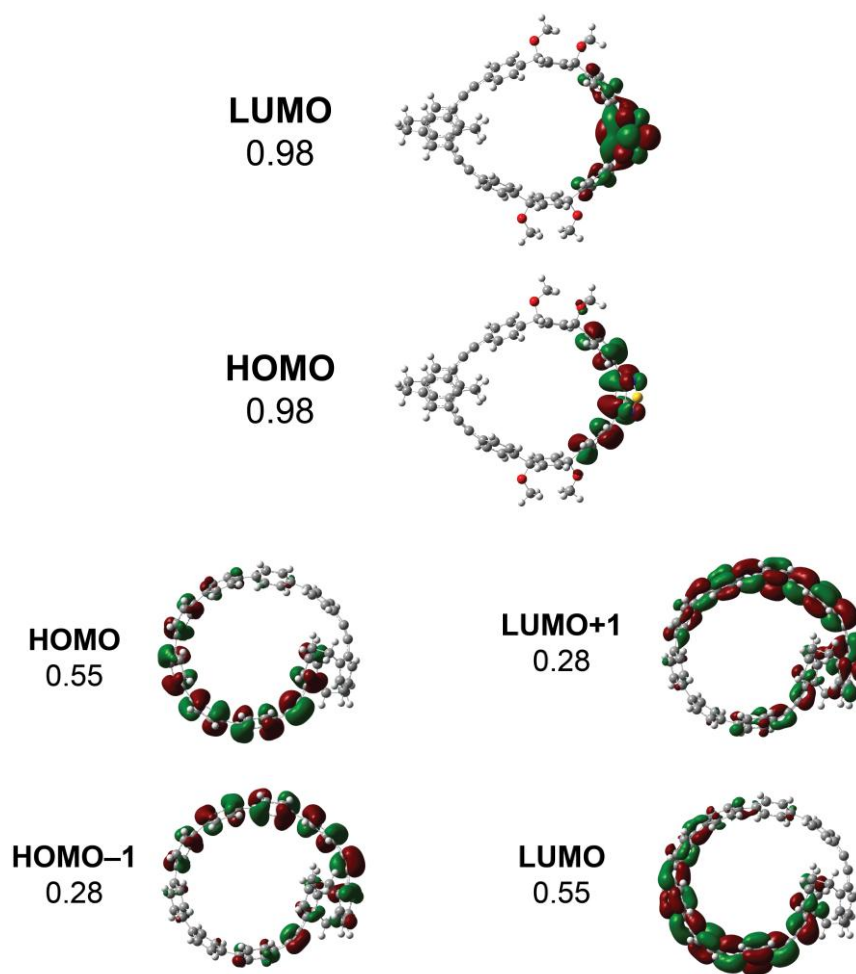


Figure A3.22. Natural transition orbitals and occupancies of the $S_0 \rightarrow S_1$ transition in $2'$ (top) and $1'$ (bottom).

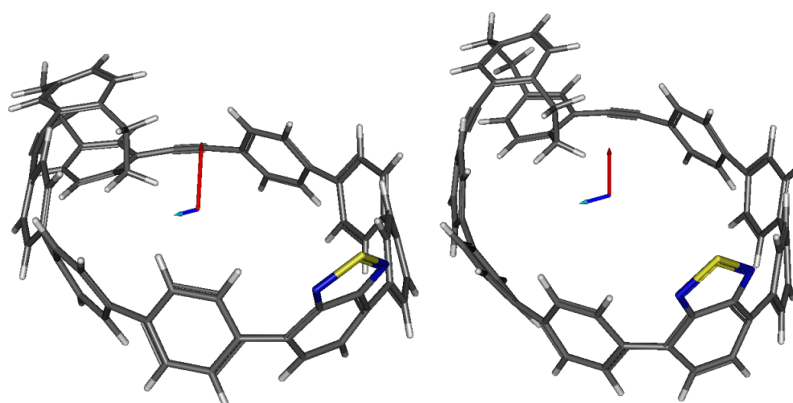


Figure A3.23. Electric (μ , blue) and magnetic (m , red) transition dipole moments of the $S_0 \rightarrow S_1$ transition (left) and $S_1 \rightarrow S_0$ transition (right) in 2 . The vectors are scaled by a factor of 2 for visualization due to small size of μ .

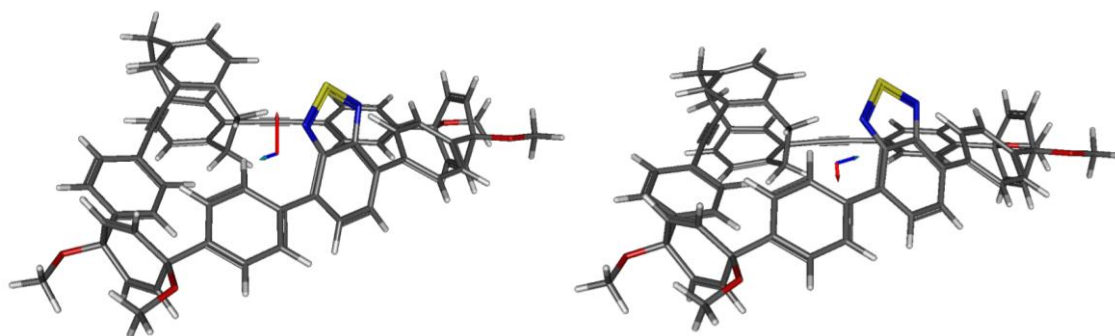


Figure A3.24. Electric (μ , blue) and magnetic (m , red) transition dipole moments of the $S_0 \rightarrow S_1$ transition (left) and $S_1 \rightarrow S_0$ transition in **3**. The vectors are scaled by a factor of 2 for visualization due to small size of μ .

Geometry of **1** was taken from ref.³³ and optimized at D3-B3LYP/6-31g(d) level of theory. **1^P** is a *pseudopara*-isomer of **1** and was optimized at the same level of theory.

Table A3.5. Calculated energies (E), oscillator strengths (f), electric (μ) and magnetic (m) transition dipole moments, and angles (θ) between them, rotatory strengths (R , velocity form), dipole strengths (D) and calculated dissymmetry factor (g_{abs}) values for **ground state** geometry of **1** and **1^P**.

Compound (Transition)	E / eV	f	$ \mu / 10^{-18} \text{ esu} \cdot \text{cm}$	$ m / 10^{-20} \text{ erg} \cdot \text{G}^{-1}$	$\theta / ^\circ$	$R / 10^{-40} \text{ esu erg cm G}^{-1}$	$D / 10^{-36} \text{ esu}^2 \text{ cm}^2 \text{ erg}^2 \text{ G}^{-2}$	$g_{abs} / 10^{-3}$
R_P - 1 ($S_0 - S_1$)	3.6809	0.2045	3.83	11.18	99.96	-735.8439	14.66	-20.08
R_P - 1^P ($S_0 - S_1$)	3.5654	0.0256	1.38	11.54	110.57	-544.6392	1.90	-114.40

Table A3.6. Calculated energies (E), oscillator strengths (f), electric (μ) and magnetic (m) transition dipole moments, and angles (θ) between them, rotatory strengths (R , velocity form), dipole strengths (D) and calculated dissymmetry factor (g_{lum}) values for 1st **excited state** geometry of **1** and **1^P**.

Compound (Transition)	E / eV	f	$ \mu / 10^{-18} \text{ esu} \cdot \text{cm}$	$ m / 10^{-20} \text{ erg} \cdot \text{G}^{-1}$	$\theta / ^\circ$	$R / 10^{-40} \text{ esu erg cm G}^{-1}$	$D / 10^{-36} \text{ esu}^2 \text{ cm}^2 \text{ erg}^2 \text{ G}^{-2}$	$g_{lum} / 10^{-3}$
R_P - 1 ($S_1 - S_0$)	2.835	0.6127	7.55	9.17	92.72	-329	57.00	-2.31
R_P - 1^P ($S_1 - S_0$)	2.834	0.5308	7.03	9.04	90.6	-66	49.39	-0.53

3.5 References

- (1) Sánchez-Carnerero, E. M.; Agarrabeitia, A. R.; Moreno, F.; Maroto, B. L.; Muller, G.; Ortiz, M. J.; de la Moya, S. Circularly Polarized Luminescence from Simple Organic Molecules. *Chem. – Eur. J.* **2015**, *21* (39), 13488–13500. <https://doi.org/10.1002/chem.201501178>.
- (2) Chen, N.; Yan, B. Recent Theoretical and Experimental Progress in Circularly Polarized Luminescence of Small Organic Molecules. *Molecules* **2018**, *23* (12), 3376. <https://doi.org/10.3390/molecules23123376>.
- (3) Li, X.; Xie, Y.; Li, Z. The Progress of Circularly Polarized Luminescence in Chiral Purely Organic Materials. *Adv. Photonics Res.* **2021**, *2* (4), 2000136. <https://doi.org/10.1002/adpr.202000136>.
- (4) Zhang, C.; Wang, X.; Qiu, L. Circularly Polarized Photodetectors Based on Chiral Materials: A Review. *Front. Chem.* **2021**, *9* (9), 711488.

- (5) Zhang, Y.; Yu, S.; Han, B.; Zhou, Y.; Zhang, X.; Gao, X.; Tang, Z. Circularly Polarized Luminescence in Chiral Materials. *Matter* **2022**, *5* (3), 837–875. <https://doi.org/10.1016/j.matt.2022.01.001>.
- (6) Tanaka, H.; Inoue, Y.; Mori, T. Circularly Polarized Luminescence and Circular Dichroisms in Small Organic Molecules: Correlation between Excitation and Emission Dissymmetry Factors. *ChemPhotoChem* **2018**, *2* (5), 386–402. <https://doi.org/10.1002/cptc.201800015>.
- (7) Nagata, Y.; Mori, T. Irreverent Nature of Dissymmetry Factor and Quantum Yield in Circularly Polarized Luminescence of Small Organic Molecules. *Front. Chem.* **2020**, *8* (8), 448. <https://doi.org/10.3389/fchem.2020.00448>.
- (8) Arrico, L.; Di Bari, L.; Zinna, F. Quantifying the Overall Efficiency of Circularly Polarized Emitters. *Chem. – Eur. J.* **2021**, *27* (9), 2920–2934. <https://doi.org/10.1002/chem.202002791>.
- (9) Rivera-Fuentes, P.; Alonso-Gómez, J. L.; Petrovic, A. G.; Seiler, P.; Santoro, F.; Harada, N.; Berova, N.; Rzepa, H. S.; Diederich, F. Enantiomerically Pure Allen–Acetylenic Macrocycles: Synthesis, Solid-State Structures, Chiroptical Properties, and Electron Localization Function Analysis. *Chem. – Eur. J.* **2010**, *16* (32), 9796–9807. <https://doi.org/10.1002/chem.201001087>.
- (10) Hasegawa, M.; Nojima, Y.; Mazaki, Y. Circularly Polarized Luminescence in Chiral π -Conjugated Macrocycles. *ChemPhotoChem* **2021**, *5* (12), 1042–1058. <https://doi.org/10.1002/cptc.202100162>.
- (11) Kubo, H.; Shimizu, D.; Hirose, T.; Matsuda, K. Circularly Polarized Luminescence Designed from Molecular Orbitals: A Figure-Eight-Shaped [5]Helicene Dimer with D₂ Symmetry. *Org. Lett.* **2020**, *22* (23), 9276–9281. <https://doi.org/10.1021/acs.orglett.0c03506>.
- (12) Warnke, I.; Furche, F. Circular Dichroism: Electronic. *WIREs Comput. Mol. Sci.* **2012**, *2* (1), 150–166. <https://doi.org/10.1002/wcms.55>.
- (13) Takaishi, K.; Iwachido, K.; Takehana, R.; Uchiyama, M.; Ema, T. Evolving Fluorophores into Circularly Polarized Luminophores with a Chiral Naphthalene Tetramer: Proposal of Excimer Chirality Rule for Circularly Polarized Luminescence. *J. Am. Chem. Soc.* **2019**, *141* (15), 6185–6190. <https://doi.org/10.1021/jacs.9b02582>.
- (14) Dhbaibi, K.; Favereau, L.; Srebro-Hooper, M.; Quinton, C.; Vanthuyne, N.; Arrico, L.; Roisnel, T.; Jamoussi, B.; Poriel, C.; Cabanetos, C.; Autschbach, J.; Crassous, J. Modulation of Circularly Polarized Luminescence through Excited-State Symmetry Breaking and Interbranched Exciton Coupling in Helical Push–Pull Organic Systems. *Chem. Sci.* **2020**, *11* (2), 567–576. <https://doi.org/10.1039/C9SC05231C>.
- (15) Dhbaibi, K.; Abella, L.; Meunier-Della-Gatta, S.; Roisnel, T.; Vanthuyne, N.; Jamoussi, B.; Pieters, G.; Racine, B.; Quesnel, E.; Autschbach, J.; Crassous, J.; Favereau, L. Achieving High Circularly Polarized Luminescence with Push–Pull Helicenic Systems: From Rationalized Design to Top-Emission CP-OLED Applications. *Chem. Sci.* **2021**, *12* (15), 5522–5533. <https://doi.org/10.1039/D0SC06895K>.
- (16) Takaishi, K.; Murakami, S.; Iwachido, K.; Ema, T. Chiral Exciplex Dyes Showing Circularly Polarized Luminescence: Extension of the Excimer Chirality Rule. *Chem. Sci.* **2021**, *12* (43), 14570–14576. <https://doi.org/10.1039/D1SC04403F>.
- (17) Uceda, R. G.; Cruz, C. M.; Míguez-Lago, S.; de Cienfuegos, L. Á.; Longhi, G.; Pelta, D. A.; Novoa, P.; Mota, A. J.; Cuerva, J. M.; Miguel, D. Can Magnetic Dipole Transition Moment Be Engineered? *Angew. Chem. Int. Ed.* **2024**, *63* (4), e202316696. <https://doi.org/10.1002/anie.202316696>.
- (18) Jasti, R.; Bhattacharjee, J.; Neaton, J. B.; Bertozzi, C. R. Synthesis, Characterization, and Theory of [9]-, [12]-, and [18]Cycloparaphenylene: Carbon Nanohoop Structures. *J. Am. Chem. Soc.* **2008**, *130* (52), 17646–17647. <https://doi.org/10.1021/ja807126u>.
- (19) Fujitsuka, M.; Cho, D. W.; Iwamoto, T.; Yamago, S.; Majima, T. Size-Dependent Fluorescence Properties of [n]Cycloparaphenylenes (n = 8–13), Hoop-Shaped π -Conjugated Molecules. *Phys. Chem. Chem. Phys.* **2012**, *14* (42), 14585. <https://doi.org/10.1039/c2cp42712e>.
- (20) Segawa, Y.; Fukazawa, A.; Matsuura, S.; Omachi, H.; Yamaguchi, S.; Irle, S.; Itami, K. Combined Experimental and Theoretical Studies on the Photophysical Properties of Cycloparaphenylenes. *Org. Biomol. Chem.* **2012**, *10* (30), 5979–5984. <https://doi.org/10.1039/C2OB25199J>.
- (21) Darzi, E. R.; Jasti, R. The Dynamic, Size-Dependent Properties of [5]–[12]Cycloparaphenylenes. *Chem. Soc. Rev.* **2015**, *44* (18), 6401–6410. <https://doi.org/10.1039/C5CS00143A>.
- (22) Xu, W.; Yang, X.-D.; Fan, X.-B.; Wang, X.; Tung, C.-H.; Wu, L.-Z.; Cong, H. Synthesis and Characterization of a Pentiptycene-Derived Dual Oligoparaphenylene Nanohoop. *Angew. Chem. Int. Ed.* **2019**, *58* (12), 3943–3947. <https://doi.org/10.1002/anie.201814482>.
- (23) Wang, L.-H.; Hayase, N.; Sugiyama, H.; Nogami, J.; Uekusa, H.; Tanaka, K. Synthesis, Structures, and Properties of Highly Strained Cyclophenylene–Ethylenes with Axial and Helical Chirality. *Angew. Chem. Int. Ed.* **2020**, *59* (41), 17951–17957. <https://doi.org/10.1002/anie.202006959>.
- (24) Sato, K.; Hasegawa, M.; Nojima, Y.; Hara, N.; Nishiuchi, T.; Imai, Y.; Mazaki, Y. Circularly Polarized Luminescence of a Stereogenic Curved Paraphenylene Anchoring a Chiral Binaphthyl in Solution and Solid State. *Chem. – Eur. J.* **2021**, *27* (4), 1323–1329. <https://doi.org/10.1002/chem.202004283>.
- (25) Nogami, J.; Nagashima, Y.; Miyamoto, K.; Muranaka, A.; Uchiyama, M.; Tanaka, K. Asymmetric Synthesis, Structures, and Chiroptical Properties of Helical Cycloparaphenylenes. *Chem. Sci.* **2021**, *12* (22), 7858–7865. <https://doi.org/10.1039/D1SC00861G>.

- (26) Wassy, D.; Hermann, M.; Wössner, J. S.; Frédéric, L.; Pieters, G.; Esser, B. Enantiopure Nano-hoops through Racemic Resolution of Diketo[n]CPPs by Chiral Derivatization as Precursors to DBP[n]CPPs. *Chem. Sci.* **2021**, *12* (30), 10150–10158. <https://doi.org/10.1039/D1SC02718B>.
- (27) Malinčík, J.; Gaikwad, S.; Mora-Fuentes, J. P.; Boillat, M.-A.; Prescimone, A.; Häussinger, D.; Campaña, A. G.; Šolomek, T. Circularly Polarized Luminescence in a Möbius Helicene Carbon Nano-hoop**. *Angew. Chem. Int. Ed.* **2022**, *61* (37), e202208591. <https://doi.org/10.1002/anie.202208591>.
- (28) Xu, Y.; Steudel, F.; Leung, M.-Y.; Xia, B.; von Delius, M.; Yam, V. W.-W. [N]Cycloparaphenylene-Pillar[5]Arene Bismacrocycles: Their Circularly Polarized Luminescence and Multiple Guest Recognition Properties. *Angew. Chem. Int. Ed.* **2023**, *62* (24), e202302978. <https://doi.org/10.1002/anie.202302978>.
- (29) Zhou, Y.; Zhang, X.; Yuan, B.; Lu, D.; Zhuang, G.-L.; Du, P. Enantiomerically Resolvable Inherent Chirality Induced by Strong *Para*-Steric Hindrance in Cycloparaphenylene-Based Carbon Nano-hoops. *Org. Lett.* **2024**, *26* (27), 5635–5639. <https://doi.org/10.1021/acs.orglett.4c01509>.
- (30) Kong, X.; Zhang, X.; Yuan, B.; Zhang, W.; Lu, D.; Du, P. Synthesis and Photophysical Properties of a Chiral Carbon Nanoring Containing Rubicene. *J. Org. Chem.* **2024**, *89* (11), 8255–8261. <https://doi.org/10.1021/acs.joc.4c00387>.
- (31) Senthilkumar, K.; Kondratowicz, M.; Lis, T.; Chmielewski, P. J.; Cybińska, J.; Zafra, J. L.; Casado, J.; Vives, T.; Crassous, J.; Favereau, L.; Stepień, M. Lemniscular [16]Cycloparaphenylene: A Radially Conjugated Figure-Eight Aromatic Molecule. *J. Am. Chem. Soc.* **2019**, *141* (18), 7421–7427. <https://doi.org/10.1021/jacs.9b01797>.
- (32) Schaub, T. A.; Prantl, E. A.; Kohn, J.; Bursch, M.; Marshall, C. R.; Leonhardt, E. J.; Lovell, T. C.; Zakharov, L. N.; Brozek, C. K.; Waldvogel, S. R.; Grimme, S.; Jasti, R. Exploration of the Solid-State Sorption Properties of Shape-Persistent Macrocyclic Nanocarbons as Bulk Materials and Small Aggregates. *J. Am. Chem. Soc.* **2020**, *142* (19), 8763–8775. <https://doi.org/10.1021/jacs.0c01117>.
- (33) He, J.; Yu, M.; Pang, M.; Fan, Y.; Lian, Z.; Wang, Y.; Wang, W.; Liu, Y.; Jiang, H. Nanosized Carbon Macrocycles Based on a Planar Chiral Pseudo *Meta*-[2.2]Paracyclophane. *Chem. – Eur. J.* **2022**, *28* (13), e202103832. <https://doi.org/10.1002/chem.202103832>.
- (34) He, J.; Yu, M.-H.; Lian, Z.; Fan, Y.-Q.; Guo, S.-Z.; Li, X.-N.; Wang, Y.; Wang, W.-G.; Cheng, Z.-Y.; Jiang, H. Lemniscular Carbon Nano-hoops with Contiguous Conjugation from Planar Chiral [2.2]Paracyclophane: Influence of the Regioselective Synthesis on Topological Chirality. *Chem. Sci.* **2023**, *14* (16), 4426–4433. <https://doi.org/10.1039/D2SC06825G>.
- (35) Lovell, T. C.; Garrison, Z. R.; Jasti, R. Synthesis, Characterization, and Computational Investigation of Bright Orange-Emitting Benzothiadiazole [10]Cycloparaphenylene. *Angew. Chem. Int. Ed.* **2020**, *59* (34), 14363–14367. <https://doi.org/10.1002/anie.202006350>.
- (36) Xue, Y.; Shi, Y.; Chen, P. Circularly Polarized Luminescent π -Conjugated Chiral Nanorings and Nanobelts. *Adv. Opt. Mater.* **2024**, *12* (12), 2303322. <https://doi.org/10.1002/adom.202303322>.
- (37) Wu, Y.; Zhuang, G.; Cui, S.; Zhou, Y.; Wang, J.; Huang, Q.; Du, P. Through-Space π -Delocalization in a Conjugated Macrocyclic Consisting of [2.2]Paracyclophane. *Chem. Commun.* **2019**, *55* (97), 14617–14620. <https://doi.org/10.1039/C9CC06492C>.
- (38) Sato, S.; Yoshii, A.; Takahashi, S.; Furumi, S.; Takeuchi, M.; Isobe, H. Chiral Intertwined Spirals and Magnetic Transition Dipole Moments Dictated by Cylinder Helicity. *Proc. Natl. Acad. Sci.* **2017**, *114* (50), 13097–13101. <https://doi.org/10.1073/pnas.1717524114>.
- (39) Xia, J.; Jasti, R. Synthesis, Characterization, and Crystal Structure of [6]Cycloparaphenylene. *Angew. Chem. Int. Ed.* **2012**, *51* (10), 2474–2476. <https://doi.org/10.1002/anie.201108167>.
- (40) Lovell, T. C.; Colwell, C. E.; Zakharov, L. N.; Jasti, R. Symmetry Breaking and the Turn-on Fluorescence of Small, Highly Strained Carbon Nano-hoops. *Chem. Sci.* **2019**, *10* (13), 3786–3790. <https://doi.org/10.1039/C9SC00169G>.
- (41) Bondarenko, L.; Dix, I.; Hinrichs, H.; Hopf, H. Cyclophanes. Part LII: Ethynyl[2.2]Paracyclophanes - New Building Blocks for Molecular Scaffolding. *Synthesis* **2004**, *2004* (16), 2751–2759. <https://doi.org/10.1055/s-2004-834872>.
- (42) Frisch, M. J.; Trucks, G. W.; Schlegel, H. B.; Scuseria, G. E.; Robb, M. A.; Cheeseman, J. R.; Scalmani, G.; Barone, V.; Mennucci, B.; Petersson, G. A.; Nakatsuji, H.; Caricato, M.; Li, X.; Hratchian, H. P.; Izmaylov, A. F.; Bloino, J.; Zheng, G.; Sonnenberg, J. L.; Hada, M.; Ehara, M.; Toyota, K.; Fukuda, R.; Hasegawa, J.; Ishida, M.; Nakajima, T.; Honda, Y.; Kitao, O.; Nakai, H.; Vreven, T.; Montgomery, J. A.; Peralta, J. E.; Ogliaro, F.; Bearpark, M.; Heyd, J. J.; Brothers, E.; Kudin, K. N.; Staroverov, V. N.; Kobayashi, R.; Normand, J.; Raghavachari, K.; Rendell, A.; Burant, J. C.; Iyengar, S. S.; Tomasi, J.; Cossi, M.; Rega, N.; Millam, J. M.; Klene, M.; Knox, J. E.; Cross, J. B.; Bakken, V.; Adamo, C.; Jaramillo, J.; Gomperts, R.; Stratmann, R. E.; Yazyev, O.; Austin, A. J.; Cammi, R.; Pomelli, C.; Ochterski, J. W.; Martin, R. L.; Morokuma, K.; Zakrzewski, V. G.; Voth, G. A.; Salvador, P.; Dannenberg, J. J.; Dapprich, S.; Daniels, A. D.; Farkas, Ö.; Foresman, J. B.; Ortiz, J. V.; Cioslowski, J.; Fox, D. J. *Gaussian 09 Revision D.01*; 2009.